Surface & Coatings Technology 205 (2010) 2031–2041

Contents lists available at ScienceDirect

Surface & Coatings Technology

journal homepage: www.elsevier.com/locate/surfcoat

Electrodeposition of Zn–Ni, Zn–Fe and Zn–Ni–Fe alloys

A. Chitharanjan Hegde [a,*,1], K. Venkatakrishna [a], N. Eliaz [b,*]

[a] Department of Chemistry, National Institute of Technology Karnataka, Srinivasnagar 575 025, India
[b] Materials and Nanotechnologies Program & School of Mechanical Engineering, Tel-Aviv University, Ramat-Aviv, Tel-Aviv 69978, Israel

ARTICLE INFO

Article history:
Received 1 March 2010
Accepted in revised form 23 August 2010

Keywords:
Zn–Ni–Fe
Electrodeposition
Anomalous codeposition (ACD)
Corrosion resistance
Mott-Schottky

ABSTRACT

Zn–Fe, Zn–Ni and Zn–Ni–Fe coatings were electrodeposited galvanostatically on mild steel from acidic baths (pH 3.5) consisted of $ZnCl_2$, $NiCl_2$, $FeCl_2$, gelatin, sulfanilic (*p*-aminobenzenesulfonic) acid and ascorbic acid. Cyclic voltammetry showed that the effect of gelatin was more pronounced than that of sulfanilic acid, and that the deposition of the ternary alloy behaved differently from the deposition of the binary alloys. In all three systems, the Faradaic efficiency was higher than 88%, the rate of Zn deposition was heavily influenced by mass-transport limitation at high applied current densities, and the deposition was of anomalous type. For each applied current density, the concentrations of Ni and Fe in the ternary alloy were higher than the corresponding concentrations in the binary alloys. The hardness of Zn–Ni coatings was the highest, while that of Zn–Fe coatings was the lowest. The Zn–Ni–Fe coatings were the smoothest, had distinguished surface morphology, and contained ZnO in the bulk, not just on the surface. The lowest corrosion rate in each alloy system (214, 325 and 26 μm $year^{-1}$ for Zn–Ni, Zn–Fe and Zn–Ni–Fe, respectively) was characteristic of coatings deposited at 30, 30 and 40 mA cm^{-2}, respectively. The higher corrosion resistance of the ternary alloy was also reflected by a higher corrosion potential, a higher impedance and a higher slope of the Mott-Schottky line. The enhanced corrosion behavior of the ternary alloy was thus attributed to its chemical composition, phase content, roughness and the synergistic effect of Ni and Fe on the *n*-type semiconductor surface film.

1. Introduction

Electrodeposited binary Zn-M alloys, where M is an iron-group metal (Fe, Co or Ni), have been studied extensively and demonstrated enhanced properties compared to pure Zn [1,2]. Because of the relatively large difference in the electronegativities of Zn and (AISI 4340) steel ($\Delta E_0 = 0.42$ V), rapid dissolution of Zn results in fairly short lifetime of the coating under corroding conditions. Alloying with an iron-group metal will bring E_0 of the coating closer to that of the substrate, thus potentially increasing the durability of the coating [3].

Zn–Ni coatings have been formed by DC plating [4–8], pulse plating [9], and as composition modulated alloys (CMA's) [10]. Zn–Fe coatings have been formed by DC plating [11–15] and as CMAs [16]. Coatings of zinc with iron-group metals have been found useful for applications such as automotive body panels, where bright corrosion resistant steel is sought [8]. The focus has been on the Zn–Ni system (8–20 wt.% Ni) due to its good corrosion resistance and enhanced mechanical properties. Yet, Zn–Fe coatings have also been used, mainly due to their low cost. Both Zn–Ni and Zn–Fe coatings are good substitutes for cadmium, which is nowadays prohibited due to its toxicity and stringent environmental regulations.

The corrosion resistance of Zn-M alloys has been found to depend significantly on the concentration of M in the deposit [17]. The use of specific bath additives has also been found beneficial with respect to corrosion resistance, even for low contents of M [18]. Ternary Zn–Ni–Fe coatings have been found to exhibit enhanced properties, including increased corrosion resistance, compared to the binary Zn–Ni and Zn–Fe alloys [19–24].

The term anomalous codeposition (ACD) was coined by Abner Brenner [25] to describe an electrochemical deposition process in which the less noble metal is deposited preferentially under most plating conditions. This behavior is typically observed in codeposition of iron-group metals, or in codeposition of an iron-group metal with Zn or Cd. In the deposition of Ni-Zn alloys, for example, adding either ion to the solution enhances the rate of deposition of the other metal [26]. Several models have been suggested to explain the ACD of Zn-M alloys [27–37]. Other behaviors have been reported by Eliaz et al. for electroplating of Ni-W [26,38,39] or Re-M [40,41] alloys.

With respect to electrodeposition of Zn-M alloys, *one model* suggests that, due to hydrogen evolution and the resulting pH increase, a zinc hydroxide film precipitates and adsorbs on the surface of the cathode. As the critical pH for precipitation of iron-group metal hydroxides is significantly higher than for precipitation of zinc hydroxide, the former may not form so that M-deposition requires

* Corresponding authors. Hegde is to be contacted at Tel.: +91 824 2474000; fax: +91 824 2474033. Eliaz, Tel.: +972 3 6407384; fax: +972 3 6407617.
E-mail addresses: achegde@rediffmail.com (A.C. Hegde), neliaz@eng.tau.ac.il (N. Eliaz).
[1] A.C. Hegde conducted some of the work at Tel-Aviv University, Israel.

0257-8972/$ – see front matter © 2010 Elsevier B.V. All rights reserved.
doi:10.1016/j.surfcoat.2010.08.102

direct discharge of M^{2+} ions through the zinc hydroxide film. At sufficiently high current densities, the high resistance of this hydroxide film favors Zn reduction while inhibiting M-deposition. This model is often termed the Hydroxide Suppression Mechanism [29,31,32,34]. A *second model* suggests that underpotential deposition (UPD) of Zn provides an alloy surface that is different from the parent metal for the continuous codeposition, thus making the deposition of the less noble component preferable [29,36]. However, if this was the case, once a monolayer is deposited, the UPD should be terminated and the ions in solution should "sense" only the last layer deposited on the surface. Hence, such a model is valid only if an alternating multilayer coating is formed, which was not the case in this study. According to a *third model*, the great difference between the exchange current densities of Zn and the iron-group metal results in a significant difference between the thermodynamic and the practical nobility. In this regard, the magnitude of the exchange current density is generally much greater for Zn compared to Ni, Co and Fe [29,30,33,34]. We recently found this model most appropriate to explain the deposition behavior in the Zn–Ni-Co system [42]. It should be noted that such a model may be proper for electroplating under galvanostatic conditions (as in our study), where a high current consumption by one element must be at the expense of another element, but may not be applicable to electroplating under potentiostatic conditions.

The present work was aimed at comparative evaluation of Zn–Ni, Zn–Fe and Zn–Ni–Fe coatings electrodeposited galvanostatically on mild steel from an acidic chloride bath containing gelatin and sulfanilic acid, with emphasis on their chemical composition, phase content, surface morphology and corrosion resistance. To the best of our knowledge, the bath compositions used in this study have not been reported before. The effect of bath additives is clarified by means of cyclic voltammetry. The comparison between the two binary alloys and the ternary alloy allows to better understand the role, individually and synergistically, of the two iron-group metals. Finally, the kinetics of alloy deposition is determined through calculations of the partial current densities. The results may be used to elucidate the model of ACD which is relevant to these specific alloy systems.

2. Experimental

Acidic baths consisting of $ZnCl_2$, $NiCl_2$, $FeCl_2$, sulfanilic acid (SA, $NH_2C_6H_4SO_3H$, IUPAC name: *p*-aminobenzenesulfonic acid), gelatin (for microbiology, CAS 9000-70-8, Merck, Mumbai) and ascorbic acid ($C_6H_8O_6$) were used (see Table 1). NH_4Cl and KCl were added to increase the conductivity and ionic strength of the electrolyte. At pH 3.5 of the baths in this study, ammonia exists in solution entirely as NH_4^+ species [26], thus the possible act of NH_3 as a complexing agent can be excluded. Ascorbic acid is a polycarboxylic acid with antioxidant properties, and is used as a chelating agent or brightener. It was used to prevent the oxidation of Fe^{2+} to Fe^{3+}. In our previous work on electrodeposition of Zn–Ni-Co [42], SA was found to improve the brightness and uniformity of coatings. Gelatin is sometimes added to zinc or other electroplating baths in order to control the deposition rate, crystallization, leveling and brightness of the deposit. Due to its very high molecular weight, its content in the plating baths in the present study represents concentrations which were several orders of magnitude smaller than the concentrations of zinc and the iron-group metal ions. Thus, it could not act as a complexing agent. The plating solutions were freshly prepared from distilled water and analytical grade reagents.

Table 1
Composition and operating conditions of optimized baths for electroplating of bright Zn–Ni, Zn–Fe and Zn–Ni–Fe alloys on mild steel.

Concentration	Zn–Ni bath	Zn–Fe bath	Zn–Ni–Fe bath
$ZnCl_2$ (M)	0.37	0.37	0.37
$NiCl_2$ (M)	0.34	–	0.34
$FeCl_2$ (M)	–	0.04	0.04
NH_4Cl (M)	2.24	2.24	2.24
KCl (M)	1.61	1.61	1.61
Ascorbic acid (g L^{-1})	–	10	5
Sulfanilic acid (M)	0.03	0.06	0.03
Gelatin (g L^{-1})	7	5	7
pH	3.5	3.5	3.5
T (°C)	30	30	30
i (mA cm^{-2}), optimized	30	30	40

Electroplating of mild steel plates was done at pH 3.5 ± 0.05 and $T = 30 \pm 2$ °C, for either 10 or 20 min (the former time – for corrosion study, the latter – for determination of chemical composition and Faradaic efficiency). The bath pH was monitored frequently and adjusted when necessary. The polished steel plates had an exposed surface area of either 7.5 or 25 cm^2 (the former – for the corrosion study) and served as a cathode. They were degreased with an alkali cleaner prior to coating. The anode was pure Zn with the same exposed area, which was placed approximately 5 cm away of the cathode. A rectangular PVC cell containing 250 cm^3 electrolyte solution was used, in conjunction with an adjustable power source. All depositions were carried out under identical stirring condition in order to maintain similar mass transport conditions near the cathode (for the same cathode dimensions). Obviously, as the overpotential is different for each metal, the partial current density (kinetics) for each metal is expected to be different too. No nitrogen (or other) purging was applied. The bath composition and operating conditions for deposition of Zn–Ni, Zn–Fe and Zn–Ni–Fe coatings were optimized by means of a standard Hull cell. The effect of each bath constituent on the appearance of the coating on a Hull cell panel was examined. While varying the concentration of one constituent in constant increments, the concentrations of all other constituents were kept constant. The concentration of a specific constituent at which the bath produced a bright, homogeneous coating, which was not peeled-off in a tape test, was fixed as its 'optimal' concentration. The procedure was repeated for all constituents, limiting the applied current density to within 10–60 mA cm^{-2}, which yielded deposits with different appearances (gray/white/black, bright/semi-bright, porous/powdery). The composition and operating conditions of optimized baths are given in Table 1.

The Faradaic efficiency (*FE*) was calculated from the mass gained, the charge passed and the chemical composition of the deposit:

$$FE = \frac{\text{measured mass gain}}{\text{theoretical mass gain}} \times 100 = \frac{w}{\frac{EW \times I \times t}{F}} \times 100 = \frac{wF}{It} \sum \frac{c_i n_i}{M_i} \times 100 \quad (1)$$

where w is the measured mass of the deposit (g), t is the deposition time (s), I is the total current passed (A), EW is the equivalent weight of the alloy (g $equiv^{-1}$), c_i is the weight fraction of the element in the alloy deposit, n_i is the number of electrons transferred per atom of each metal, M_i is the atomic mass of that element (g mol^{-1}), and F is the Faraday's constant (96,485 C mol^{-1}). While the thickness of the coating was estimated by Faraday's law, it was verified by measurements, using a digital thickness meter (Coatmeasure model M & C). The partial deposition current densities were calculated (in units of A cm^{-2}) from the mass gained and the chemical composition of the deposit, using the equation:

$$i_i = \frac{w}{At} \times \frac{c_i n_i F}{M_i} \quad (2)$$

where A is the surface area of the cathode (cm^2).

Cyclic voltammetry (CV) was performed in a conventional three-electrode cell in order to better understand the process of electrodeposition in each of the three systems and to identify the effects of

gelatin and SA. The bath composition and pH was as in Table 1. Before carrying out the experiments, the bath temperature was stabilized at 30 °C. All chemicals used were of analytical grade. Double distilled water was used for preparation of the electrolyte solutions. Pure platinum foil with a surface area of 1 cm^2 was used as working electrode. Although this is a different material than the steel substrate used for galvanostatic deposition, it enabled elimination of noise in the CV experiments. Furthermore, it may be argued that once several nanometers of coating material are deposited, the substrate no longer has any effect on the deposition process. Before each experiment, the electrode was activated by immersion in dilute HNO_3. The CV experiments were conducted in a quiescent solution, without purging. A scan rate of 10 mV s^{-1} was selected based on preliminary experiments. The scan began from 0 V in the positive direction, up to +1.0 V. Then, it was reversed to the negative direction, down to −1.4 V, and finally reversed back to +1.0 V. The potentials were measured versus a saturated calomel reference electrode (SCE).

The aqueous corrosion behavior of the coatings was studied by the potentiodynamic polarization and electrochemical impedance spectroscopy (EIS) techniques. The corrosion current density and corrosion potential were determined based on Tafel's extrapolation. The exposed surface area of all samples was 1 cm^2. A standard three-electrode cell containing 5% analytical grade sodium chloride (NaCl) at 25 °C was used. The potential was measured versus SCE, whereas Pt mesh was used as a counter electrode. An Electrochemical Work Station (PGSTAT 30 from Metrohm) was used and applied a scan rate of 1 mV s^{-1}, from −0.5 V vs. open-circuit potential (OCP) to +1.0 V vs. OCP. The EIS measurements were run from 100 kHz to 10 mHz, and the Nyquist plots were analyzed. The electronic properties of the corrosion product films were probed *in situ* by the Mott-Schottky analysis.

Characterization of the coatings was done by a variety of analytical facilities. The surface morphology of the deposits was observed by means of an environmental scanning electron microscope (ESEM, Quanta 200 FEG from FEI). The attached liquid-nitrogen-cooled Oxford Si energy dispersive spectroscopy (EDS) detector was used to determine the atomic composition of the alloy. Each sample was analyzed at five locations, to confirm uniformity. Some work was done using JEOL 6805LA scanning electron microscope and the EDS detector attached to it. The composition of the alloys was also measured by stripping the deposit of known mass into dilute HCl solutions followed by colorimetric (spectrophotometric) analysis [43]. In this method, the corresponding metal ions, under proper pH conditions, are made to form a colored complex, by addition of a complexing agent (dimethyl glyoxime in the case of Zn–Ni, nitroso-R salt in the case of Zn-Co). The amount of Ni or Co present in the solution can be evaluated from their respective standard plots, based on the Beer-Lambertz equation. While this procedure is useful for analysis of the binary alloys, it could not be applied in the case of the ternary alloy due to interference between and Ni and Fe ions. Hence, atomic absorption spectroscopy (AAS) in a graphite furnace was used in that case. In order to allow comparison between data acquired by different analytical techniques, the data obtained for the binary alloys by means of the colorimetric method were cross-verified by data from AAS; good agreement was found between results from these two techniques. X-ray Photoelectron Spectroscopy (XPS) measurements were performed in UHV (2.5×10^{-10} Torr base pressure), using a 5600 Multi-Technique System (PHI, USA). The samples were irradiated with an Al-K_α monochromated source, and the emitted electrons were analyzed by a spherical capacitor analyzer. Analysis was made at the surface as well as after sputter cleaning with 4 kV Ar^+ ion gun. Charging was compensated with charge neutralizer. The binding energy (BE) of adventitious carbon at 285 eV was taken as an energy reference for the measured peaks. A low-resolution survey spectrum was taken over a wide energy range, in order to identify the elements present at the sample surface. High-resolution spectra were then acquired at pass energy of 23.5 eV, at an increment of 0.05 eV $step^{-1}$. The surface morphology of the coatings was also studied in air by atomic force microscope (AFM, PicoSPM™ from Molecular Imaging). Imaging was done under contact mode, using tips made of Si_3N_4. Topography, deflection and 3D images were acquired. Roughness parameters were calculated by image processing with the aid of SPIP™ ver. 3.0.0.11 software from Image Metrology A/S. The hardness of 20 μm thick coatings was measured using a computer-controlled micro-hardness tester (model MMT-X7 from Clemex) and the Vickers test.

3. Results and discussion

3.1. The effect of gelatin and SA on the cyclic voltammograms

The authors recently studied by CV the role of these additives in the case of the Zn–Ni-Co system and its binary sub-systems [42]. Due to some similarities, the role of these additives in the case of the Zn–Ni–Fe system is discussed here briefly. The standard potentials of Zn, Ni and Fe are −0.76, −0.25 and −0.44 V vs. SHE, respectively. For the respective ion concentrations as in Table 1, and neglecting the activity coefficients and the possible effect of a ligand, the reversible potentials for deposition of these metals at 30 °C are −1.02, −0.51 and −0.72 V vs. SCE, respectively, according to the Nernst equation.

Fig. 1a shows the cyclic voltammograms obtained for Zn–Ni on Pt. Without additives, the deposition Zn(II)→Zn(0) started at approximately −1.15 V, while hydrogen evolution was indicated by c2. The anodic sweep showed two dissolution peaks – a2 related to Zn dissolution from the α phase (a solid solution of Zn in Ni with an fcc structure), and a1 related to the dissolution of the porous Ni matrix left after the preferential dissolution of Zn from the Zn-rich phases. The addition of SA shifted the deposition potential in the negative direction, starting at around −1.21 V, and made the peak c1 more distinct, thus reflecting an increase in the FE. The displacement of c1 to a more negative value due to the presence of SA represents cathodic polarization, and may be related to the adsorption of SA onto the Pt surface. In the anodic sweep, a shoulder a'2 appeared at −0.8 V, while the area (charge) below a2 decreased, thus possibly reflecting the presence (and dissolution) of a second Zn-rich phase. The presence of gelatin changed the shape of the voltammograms in two ways: (i) the deposition potential was shifted to slightly less negative value (starting at around −1.13 V) while the deposition current density was decreased, and (ii) the intensity of a1 was reduced, a2 disappeared, and a new peak (a3) appeared at −0.89 V, jointly with a shoulder a'2. The peak a3 may be related to the η (a solid solution of Ni in Zn with a hexagonal crystal structure, containing up to 1 at.% Ni) and γ (an intermetallic compound Ni_5Zn_{21} with a bcc structure) phases [42]. The effect of gelatin was more pronounced than that of SA in the bath containing both of these additives. It seems that gelatin affected the deposition process through preferential adsorption on the surface of the cathode. In Fig. 1a it is also evident that when the scan was reversed at −1.4 V, two crossovers appeared, known as the nucleation overpotential (E_η) and the crossover potential (E_{co}). The appearance of these two crossovers is characteristic of processes that involve the nucleation of a new phase [42].

In the case of the Zn–Fe system (Fig. 1b) without additives, the deposition started at around −1.08 V (peak c1). In the anodic sweep, two peaks are evident – a2 at −0.95 V which may be related to dissolution of pure Zn and/or Zn from the η phase, and a1 at −0.58 V that may be attributed either to dissolution of pure Fe or to dissolution of Zn from the γ phase. When SA was added, the deposition potential did not change. The oxidation peaks slightly shifted, to −0.92 and −0.59 V, respectively. While the area (charge) below a2 increased, that below the a1 decreased. The presence of gelatin in the bath apparently changed the shape of the voltammograms. The deposition started at −1.14 V and the deposition current density decreased. In

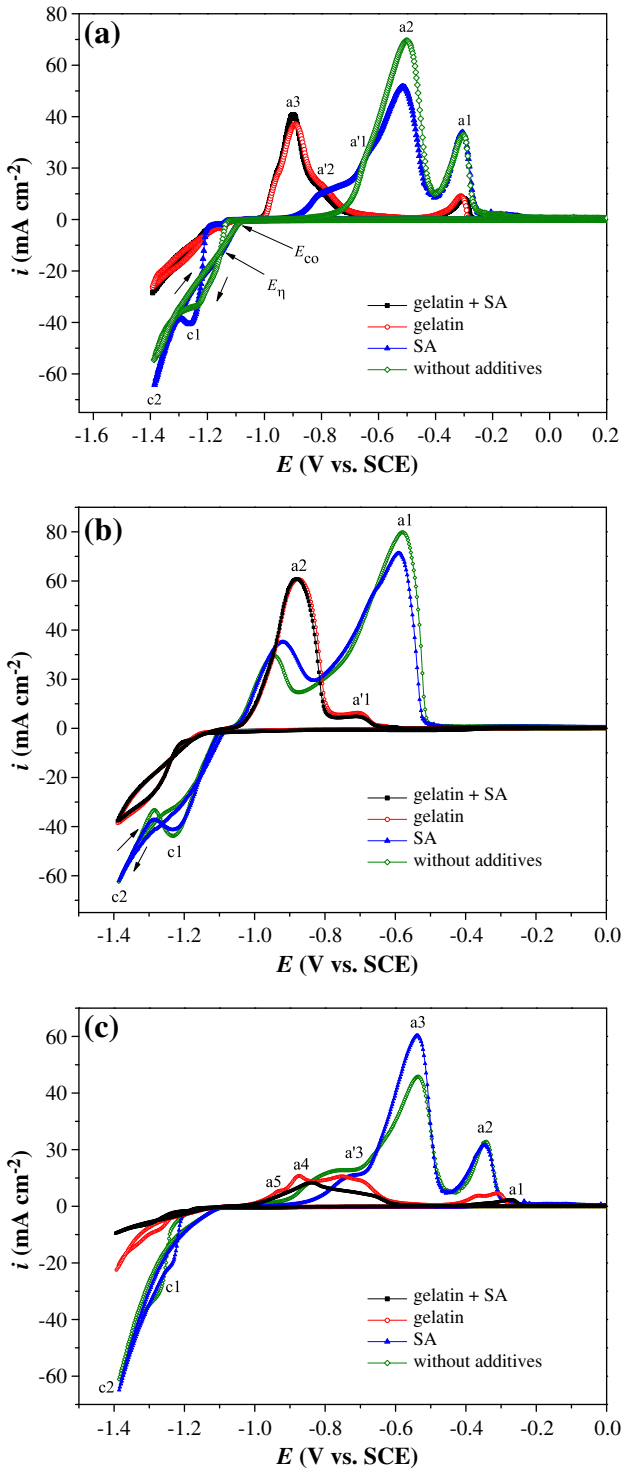

Fig. 1. Cyclic voltammograms for (a) Zn–Ni [42], (b) Zn–Fe, and (c) Zn–Ni–Fe baths, demonstrating the effects of gelatin and sulfanilic acid. Working electrode: Pt, $T = 30$ °C, $\upsilon = 10$ mV s^{-1}, pH 3.5.

the anodic sweep, a2 was shifted to −0.87 V and the associated charge increased. In contrast, a1 became a shoulder a'1 with significantly reduced intensity and was shifted to −0.68 V. This change may indicate that the fraction of the η phase in the alloy increased as a result of gelatin addition. When both gelatin and SA were present in the bath, gelatin apparently dictated the shape of the voltammogram, namely the deposition potential and the oxidation peaks were the same.

Fig. 1c shows the cyclic voltammograms obtained for the Zn–Ni–Fe bath. These voltammograms are different than those of the binary alloys. Without any additives, the deposition potential was at around −1.18 V (peak c1). A shoulder a'3 and two oxidation peaks a3 and a2 appeared at −0.77 V (may be related to dissolution of Zn from the η phase), −0.53 V (may be attributed either to dissolution of pure Fe or to dissolution of Zn from the γ phase), and −0.34 V (may be related to dissolution of pure porous Ni or Fe), respectively. The addition of SA nearly did not affect the deposition potential, but a'3 was shifted to −0.72 V, with a reduction in the associated charge. The charge associated with a3 increased although its potential remained essentially the same. The second oxidation peak (a2) essentially did not change. The presence of gelatin changed the behavior in this system too. The deposition potential was approximately −1.21 V, but the associated current density decreased. In the anodic sweep, a new small peak a5 appears at −0.93 V, followed by oxidation peaks at −0.87 (a4), −0.75, −0.36, and −0.31 V. The intensity of the oxidation peaks decreased. When both SA and gelatin were present in the bath, the deposition potential was as that in the presence of gelatin only. However, only two oxidation peaks are evident, at −0.84 (broad) and −0.27 V, respectively. In the presence of both additives, the charge associated with the anodic reactions decreased, thus possibly indicating improved corrosion resistance.

Thus, it may be concluded that gelatin affected the deposition process more than SA, and that the deposition of the ternary alloy was different from that of the binary alloys. With regard to the second conclusion, the behavior of the Zn–Ni–Fe system is different from that previously reported [42] for the Zn–Ni-Co system. It should also be recalled that the kinetics of the hydrogen evolution reaction on Zn is slower than that on Ni or Fe.

3.2. The effect of current density on the Faradaic efficiency, appearance and chemical composition of the coating

The applied current density affected the appearance, chemical composition and corrosion resistance of the coatings, as evident in Tables 2, 3, and 4. Both Zn–Ni and Zn–Fe baths produced semi-bright deposit at low current density and porous bright deposits at high current density. The effects of the applied current density on the *FE* and on the chemical composition of Zn–Ni, Zn–Fe and Zn–Ni–Fe alloys are shown in Fig. 2a–c, respectively. The mass gain measured in each case is listed in Tables 2, 3 and 4, respectively. In all cases, the *FE* was higher than 88%. Generally speaking, the *FE* was slightly lower at high current density.

In all three systems, as the current density was increased, the concentration of the nobler (iron-group) metal in the coating increased too (Fig. 2). There is no reason to assume that the different behavior of the composition of Zn–Ni at $i = 10$ mA cm^{-2} is associated with a transition to non-anomalous codeposition at low current densities, such as that reported for Zn-M systems [25,35]. It has been reported elsewhere too that increase of the applied current density resulted in an increase of the content of the nobler metal in the coating [44–46]. It could be speculated that a change in the applied current density leads to a change in the local pH, thus affecting the

Table 2
The effects of applied current density on the mass gain, thickness and hardness of Zn–Ni coatings, as well as on their corrosion characteristics [42].

i (mA cm^{-2})	w (mg)	VHN	t (μm)	E_{corr} (−V vs. SCE)	i_{corr} (μA cm^{-2})	CR (μm year^{-1})
10	93.2	172	7.6	1.063	39.5	567
20	193.1	197	15.9	1.083	31.7	455
30	289.6	220	20.5	1.142	14.9	214
40	379.8	214	25.0	1.097	18.0	258
50	467.7	205	27.8	1.089	36.4	522

Table 3
The effects of applied current density on the mass gain, thickness and hardness of Zn–Fe coatings, as well as on their corrosion characteristics.

i (mA cm^{-2})	w (mg)	VHN	t (μm)	E_{corr} (−V vs. SCE)	i_{corr} (μA cm^{-2})	CR (μm year^{-1})
10	92.0	145	5.2	1.128	38.8	559
20	187.5	171	10.5	1.194	26.4	380
30	269.9	175	15.1	1.206	22.6	325
40	356.2	177	19.9	1.144	28.7	414
50	433.2	189	24.2	1.127	34.9	502

stability of complexes of the iron-group metal that have direct effect on the composition of the coating.

Comparing between the binary alloy systems, at each current density the concentration of Ni in the coating was higher than that of Fe. This may be related to the nobler (less negative) standard potential of Ni compared to Fe, higher atomic mass of Ni compared to Fe (58.71 versus 55.85 g mol^{-1}, respectively), and higher concentration of the nickel ion in solution. Both concentrations of Ni and Fe in the ternary alloy increased as the current density was increased. Moreover, for each current density, the concentration of each element in the ternary alloy was higher than its corresponding concentration in the binary alloy. This means that there could be a synergistic catalytic effect due to their co-presence in solution.

The high concentration of the less noble metal (Zn) in the coatings reflects anomalous codeposition [25]. It should be noted that the Zn/M ion ratio in the bath solution was 1.09, 9.25 and 0.97 in the case of Zn–Ni, Zn–Fe and Zn–Ni–Fe systems, respectively (i.e. always much lower than the corresponding ratio between the concentration of elements in the coating).

Fig. 3 shows the dependence of the partial current densities of Zn, Ni and Fe on the applied current density. It is evident that in all cases, the partial current densities increased as the applied current density was increased. It is also evident that in all three alloy systems the partial current density of Zn is always much higher than those of the iron-group metals. The partial current density of Zn in the case of the ternary alloy decreased compared to that in the case of the binary alloys, whereas the partial current densities of the iron-group metals increased. This supports the possibility of a synergistic catalytic effect of Ni on Fe and vice versa. Dividing the sum of the partial current densities of Zn, Ni and Fe by the applied current density resulted in values essentially identical to those of the *FE* shown in Fig. 2. It is assumed that the partial current density of the hydrogen evolution reaction would complement this ratio to nearly 100%.

In order to determine how far the actual partial deposition current densities of Zn, Ni and Fe were from the respective limiting current densities i_L, the following experiment was conducted. Potentiodynamic polarization scans were used to determine the limiting current density i_L of each metal separately, under exactly the same conditions of cell configuration, area of electrodes and stirring, but at a concentration that was 10 times lower than the actual concentration listed in Table 1. The measured i_L value was then multiplied by 10, to obtain the actual i_L during deposition. Thus, i_L values of 39.8, 42.8 and 5.6 mA cm^{-2} were measured for Zn, Ni and Fe, respectively. Next, the

Table 4
The effects of applied current density on the mass gain, thickness and hardness of Zn–Ni–Fe coatings, as well as on their corrosion characteristics.

i (mA cm^{-2})	w (mg)	VHN	t (μm)	E_{corr} (−V vs. SCE)	i_{corr} (μA cm^{-2})	CR (μm year^{-1})
10	91.0	148	6.2	1.298	8.4	122
20	183.8	178	11.8	1.287	5.3	77
30	276.3	185	16.2	0.726	3.0	43
40	370	197	20.6	0.812	1.8	26
50	453.4	205	25.5	0.977	2.4	35
60	539.5	212	28.4	1.112	6.8	98

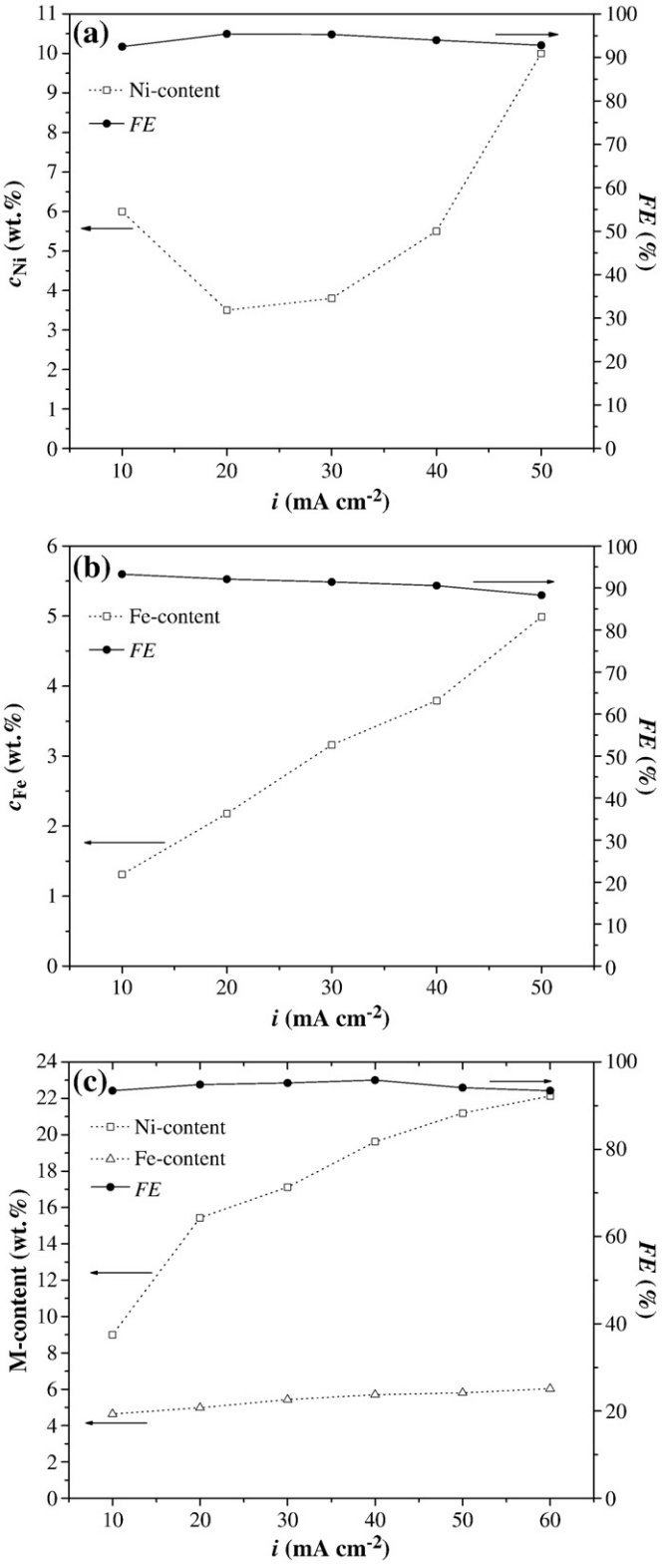

Fig. 2. The dependence of Faradaic efficiency (solid symbols, solid lines) and the iron-group metal content of the deposit (empty symbols, dot lines) on current density. Plating was conducted for 20 min at pH 3.5 and $T = 30$ °C on steel with an exposed area of 25 cm^2. (a) Zn–Ni [42], (b) Zn–Fe, and (c) Zn–Ni–Fe. Chemical composition was determined either by colorimetric analysis (binary alloys) or by AAS (ternary alloy).

partial deposition current densities (Fig. 3) were divided by the respective limiting current densities. Thus, for the Zn–Ni system, it was found that the $i_{Zn}/i_{L,Zn}$ increased from 0.22 to 1.0, while $i_{Ni}/i_{L,Ni}$ increased from 0.01 to 0.12, as the applied current density was raised

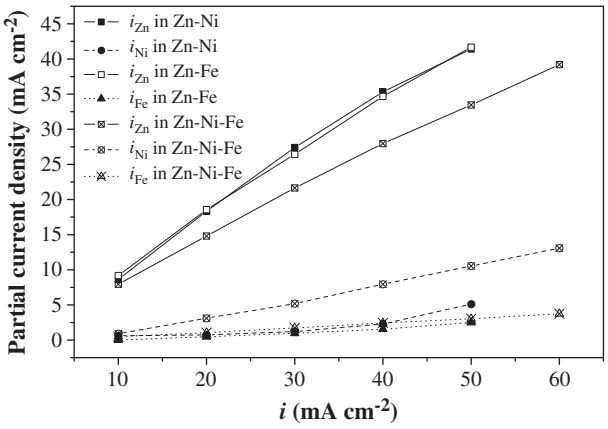

Fig. 3. The dependence of the partial current densities of Zn, Ni and Fe on the applied current density. Plating was conducted for 20 min at pH 3.5 and $T = 30$ °C on steel with an exposed area of 25 cm^2. Chemical composition was determined either by colorimetric analysis (binary alloys) or by AAS (ternary alloy).

from 10 to 50 mA cm^{-2}. Similarly, in the case of the Zn–Fe system, $i_{Zn}/i_{L,Zn}$ increased from 0.24 to 1.0, while $i_{Fe}/i_{L,Fe}$ increased from 0.003 to 0.44, as the applied current density was raised from 10 to 50 mA cm^{-2}. In the case of the Zn–Ni–Fe system, $i_{Zn}/i_{L,Zn}$ increased from 0.21 to 0.88, while $i_{Ni}/i_{L,Ni}$ increased from 0.01 to 0.22 and $i_{Fe}/i_{L,Fe}$ increased from 0.09 to 0.54, as the applied current density was raised from 10 to 50 mA cm^{-2}. These results show that, in all cases, the rate of Zn deposition was heavily influenced by mass-transport limitation at high applied current densities, while the rates of Ni and Fe deposition were not.

3.3. The thickness and hardness of the coatings

The thickness of all alloy coating systems was found to increase as the applied current density was increased (see Tables 2–4). Such a thickness increase is expected when the FE is essentially constant. The hardness either increased with current density (Zn–Fe and Zn–Ni–Fe), or increased to a peak value and then decreased (Zn–Ni). The hardness of the Zn–Ni coatings was higher than that of the Zn–Fe coatings. The hardness of the Zn–Ni–Fe coatings was slightly higher than that of Zn–Fe coatings, but lower than that of Zn–Ni coatings. As the *FE* values are similar in the three alloy systems, the difference in hardness may not be related to the absorption of hydrogen. Instead, it may be related to the atomic radii of the three elements (1.38, 1.26 and 1.24 Å for Zn, Fe and Ni, respectively) and the resulting mismatch strains.

3.4. The surface morphology of the coatings

The ESEM images in Fig. 4a–c reveal the typical surface morphologies of optimized Zn–Ni, Zn–Fe and Zn–Ni–Fe coatings. The coatings do not contain surface cracks, even at lower magnifications (not shown). The addition of Fe seem to improve the uniformity of the coating (this is more distinct at low magnifications). The Zn–Ni coating (Fig. 4a) shows dendritic growth that indicates on a mass transport-controlled electrocrystallization process. The Zn–Fe coating (Fig. 4b) also exhibits dendritic growth, but with larger dendrites. The surface morphology of the Zn–Ni–Fe coating (Fig. 4c) is much different and consists of bars with rectangular cross-section. This granular morphology may be attributed to the higher concentrations of Ni and Fe in the deposit.

Fig. 5a–c show the 2D deflection and 3D images of Zn–Ni, Zn–Fe and Zn–Ni–Fe, respectively. The mean roughness R_a was determined based on AFM images using the SPIP™ software. The R_a values were 34.5, 14.3 and 6.7 nm for Zn–Ni, Zn–Fe and Zn–Ni–Fe, respectively. Thus, it may be concluded that the ternary alloy coating is smoother

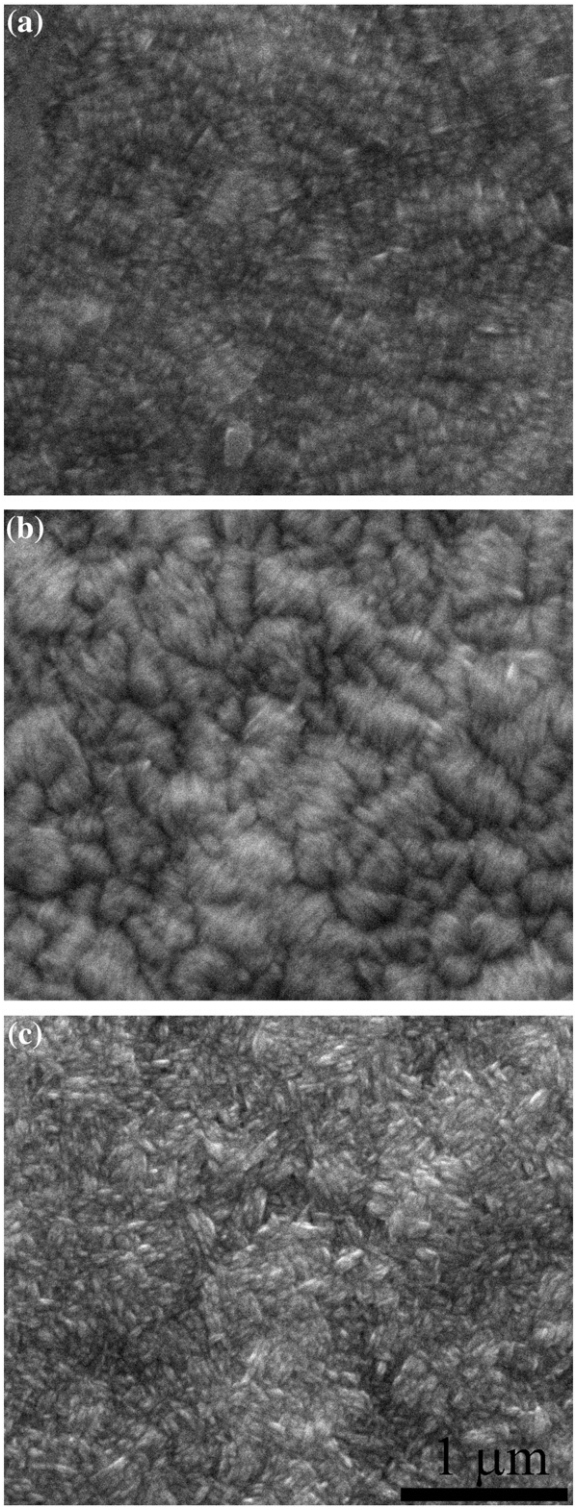

Fig. 4. ESEM images demonstrating the typical surface morphology of optimized (a) Zn–Ni, (b) Zn–Fe, and (c) Zn–Ni–Fe coatings.

than the binary alloy coatings. The Abbott-Firestone curves revealed that the ternary alloy coating was the smoothest, and it also had the most uniform roughness distribution.

3.5. Surface chemistry of the coatings

XPS measurements were made. Fig. 6 presents selected spectra of zinc before and after sputter cleaning. It is difficult to discriminate

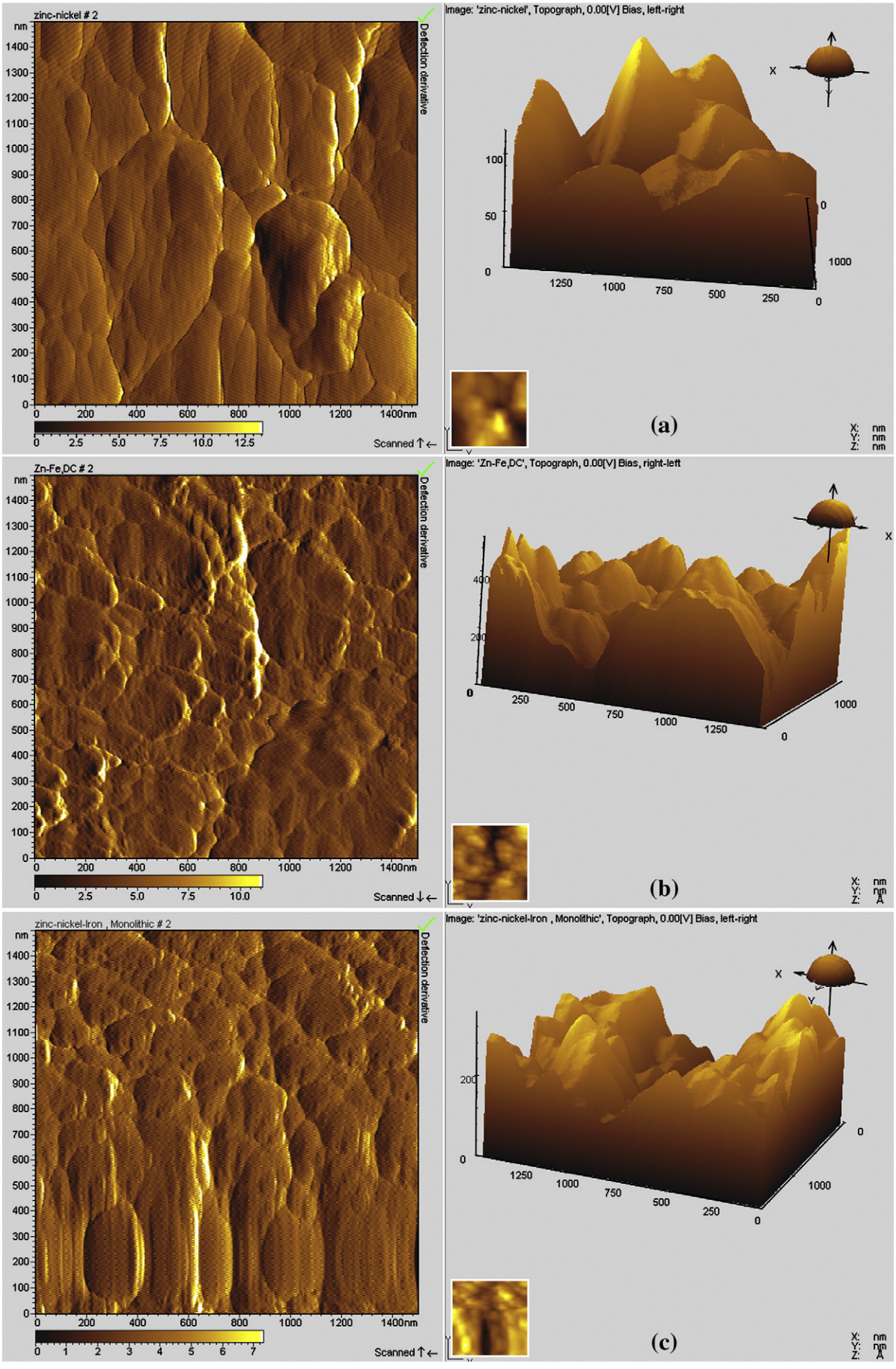

Fig. 5. AFM 2D deflection (left) and 3D (right) images of optimized (a) Zn–Ni, (b) Zn–Fe, and (c) Zn–Ni–Fe coatings.

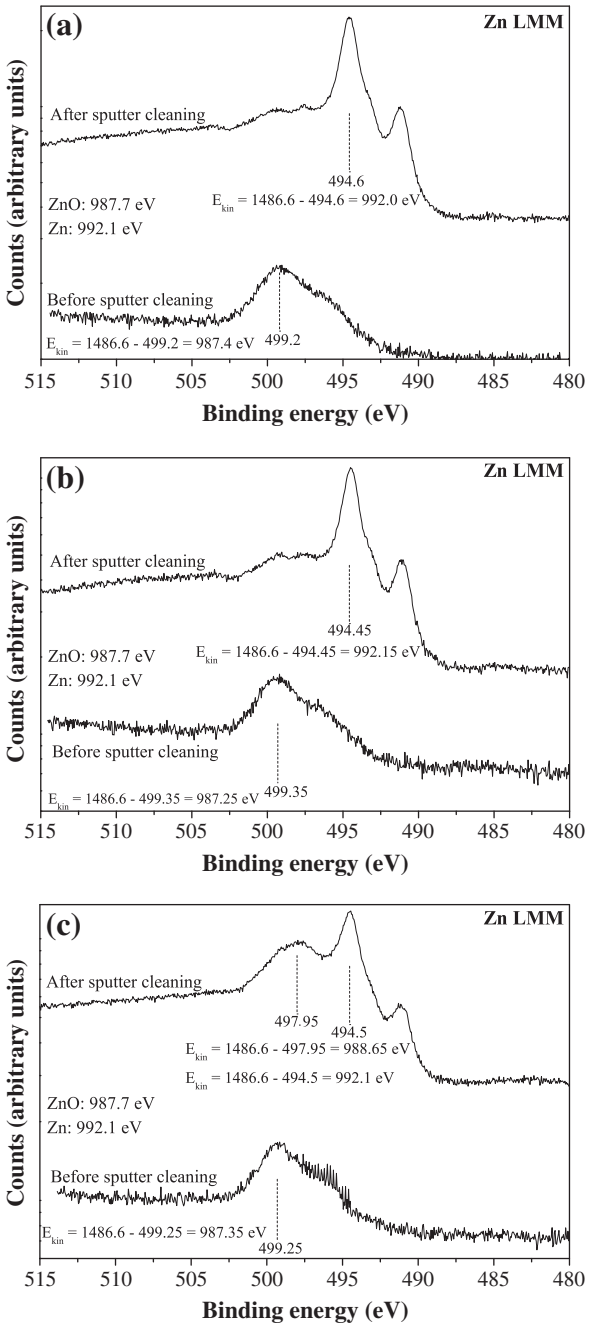

Fig. 6. XPS spectra showing the Zn LMM peak before and after sputter cleaning for: (a) Zn–Ni, (b) Zn–Fe, and (c) Zn–Ni–Fe.

between non-oxidized zinc and oxidized zinc because the Zn $2p_{3/2}$ spectra are similar for both states (1021.6 eV and 1021.7 eV, respectively) [29]. To overcome this problem, the Auger spectrum of Zn($L_3M_{45}M_{45}$) was recorded and reported in Fig. 6. The chemical compositions after sputter cleaning are summarized in Table 5. Before sputter cleaning, the Zn–Ni and Zn–Fe alloys showed only C, O, Zn and N (in descending order) at the surface. The surface composition was similar in both cases. The Zn–Ni-Fe alloy showed these four elements at the surface, in addition to small amount (0.15 at.%) of Fe. Its surface composition was not significantly different than that of the binary alloys. After sputter cleaning (Table 5), N disappeared and C significantly reduced, as expected. In the case of the binary alloys, either Ni or Fe appeared. In both cases, the concentration of oxygen was significantly lower than that in the ternary alloy. Thus, the ternary

Table 5
Atomic concentration of elements (%) after sputter cleaning.

	Zn–Ni	Zn–Fe	Zn–Ni–Fe
Zn	79.84	82.36	67.78
Ni	9.18	–	3.92
Fe	–	2.50	0.24
O	8.69	12.13	25.87
C	2.29	3.00	2.18

The data refer to samples deposited under optimal current density ($i = 30$ mA cm^{-2} for Zn–Ni and Zn–Fe, $i = 40$ mA cm^{-2} for Zn–Ni–Fe).

alloy may be oxidized even after sputter cleaning. In addition, the concentration of Zn was significantly lower in the ternary alloy compared to the binary alloys.

Fig. 6 shows that while zinc is present at the surface of the Zn–Ni coating before sputter cleaning in the oxidized (ZnO) state, in the bulk material it is present in the non-oxidized (Zn) state. The same behavior is evident in the case of Zn–Fe. On the other hand, while ZnO is present at the surface of the Zn–Ni–Fe coating before sputter cleaning, the bulk material contains both Zn and ZnO.

3.6. The phase composition of the coatings

Fig. 7 shows the XRD patterns for Zn–Ni, Zn–Fe and Zn–Ni–Fe coatings on steel. It is well known that electrodeposits often contain metastable phases, or phases that are either deficient or oversaturated compared to their counterparts in the equilibrium phase diagram. Electrodeposits of Zn–Ni alloys may contain an η phase (a solid solution of Ni in Zn), a γ phase (an intermetallic compound Ni_5Zn_{21}), an α phase (a solid solution of Zn in Ni), and sometimes even a δ phase (an intermetallic compound Ni_3Zn_{22}) [47–49]. In Fig. 7, the reflections in the pattern of Zn–Ni belong to the steel substrate, minor γ phase, and major η phase with crystal orientation (103). The co-existence of two Zn–Ni phases is in accordance with Fig. 1a. Electrodeposits of Zn–Fe alloys may contain η (hcp), δ (hcp), Γ (bcc), $Γ_1$ (fcc), α (bcc) and ζ (monoclinic) phases [50–53]. In Fig. 7, the reflections in the pattern of Zn–Fe are similar to those in the pattern of Zn–Ni, except that the η(110) reflection becomes the strongest (i.e. there is a change in crystal orientation). In this pattern, the Fe reflections may be related not only to the substrate, but also to the coating (as pure Fe may be present, according to Fig. 1b). In addition, based on Fig. 1b it cannot be excluded that some of the reflections belong to pure Zn and not to η. In the case of Zn–Ni–Fe, the crystal orientation is as in the case of Zn–Fe. However, new reflections appear, which can be related to ZnO, in accordance with the XPS results.

3.7. Corrosion resistance

Data on the corrosion potential (E_{corr}), corrosion current density (i_{corr}) and corrosion rate (*CR*) of Zn–Ni, Zn–Fe and Zn–Ni–Fe alloys are summarized in Tables 2, 3 and 4, respectively. The lowest *CR* in each alloy system (214, 325 and 26 μm year^{-1} for Zn–Ni, Zn–Fe and Zn–Ni–Fe, respectively) was characteristic of coatings deposited at 30, 30 and 40 mA cm^{-2}, respectively. For applied current densities between 10 and 50 mA cm^{-2}, the variation in E_{corr} was maximal in the case of the ternary alloy system (572 mV versus 79 mV in the case of the binary alloys). The lower *CR* of the ternary alloy coating compared to the binary alloy coatings may be related to its significantly higher content of iron-group metals and to the presence of ZnO in the former, as indicated by both XPS and XRD data. Potentiodynamic polarization curves of the three alloy coatings deposited at their optimal current density are presented in Fig. 8. The ternary alloy exhibits the highest corrosion potential and the lowest corrosion current density (based on Tafel extrapolation), namely enhanced corrosion performance. In Fig. 1, the change in the intensities of the oxidation peaks reflects different relative contents of the η and γ phases in the alloy. It should

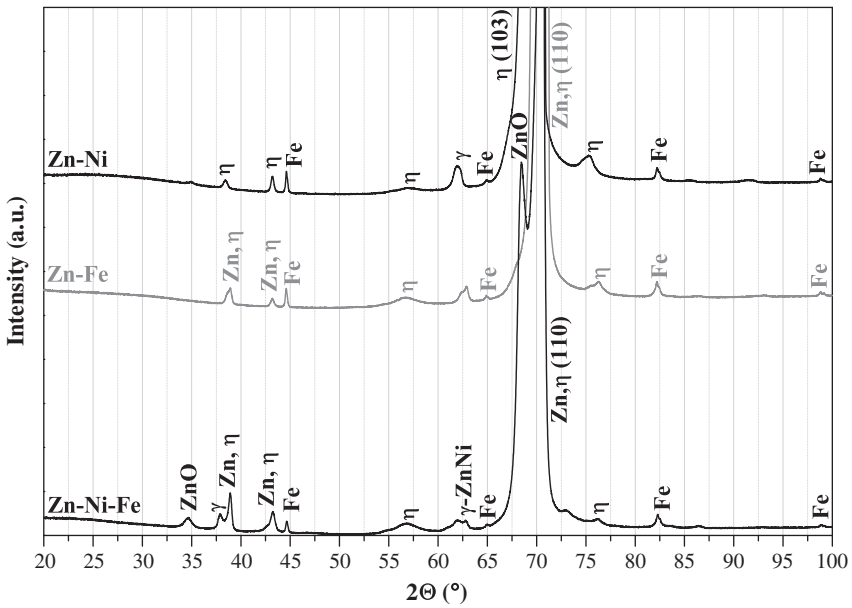

Fig. 7. XRD patterns typical of Zn–Ni, Zn–Fe and Zn–Ni–Fe coatings on steel.

be noted that a lower η-to-γ content ratio should result in improved corrosion resistance, as the γ phase is nobler.

EIS is a useful technique for ranking coatings [54,55]. Fig. 9 shows the EIS Nyquist plots of the three alloys in 5% NaCl solution, where $Z'(\omega)$ and $Z''(\omega)$ are the real and imaginary parts of the measured impedance, respectively, and ω is the angular frequency. The significantly higher impedance and larger diameter of the (incomplete) semicircle in the spectra of the ternary alloy reflect its higher corrosion resistance, which can be related to a change in the film (coating) capacitance C_f, and not only control by the charge transfer resistance R_{ct}. The capacitive impedance at high frequencies is well related to the thickness and the dielectric constant of the coating. The decrease in this constant for the Zn–Ni–Fe alloy reflects its higher corrosion resistance. An inductive loop is evident on the low-frequency side, but Warburg impedance (which reflects a diffusion-limited process) is not. For each alloy system, the impedance and the diameter of the semicircle were the largest in the case of a coating deposited at the optimal conditions. In certain cases, two semicircles appeared in the spectra (e.g. in the case of Zn–Ni deposited at 20 mA cm^{-2} or Zn–Fe deposited at 40 mA cm^{-2}), representing two relaxation processes – one in the high- and one in the low-frequency range. It is well known that the capacitance of oxide layer is typically very low, and their impedance response usually appears in the high-frequency range. The high-frequency time constant could thus be attributed to the formation of a porous oxide layer (corrosion product), while the low-frequency time constant should be related to the activation process itself.

The most common *in situ* method for probing the electronic properties of the corrosion product film is the Mott-Schottky analysis [42,56]. Fig. 10 shows the Mott-Schottky plot for the ternary Zn–Ni–Fe coating. It is evident that the surface film behaves like an *n*-type semiconductor (a positive slope). Hong et al. [57] explained the corrosion behavior of pure Ti versus Ti-Ag alloy in terms of an *n*-type semiconductor containing oxygen vacancies, the migration of which controls the kinetics of corrosion in neutral solutions. The slope of the straight line in Fig. 10 (5.18×10^8 F^{-2} V^{-1}) is much higher than the corresponding slopes of the lines for the binary Zn–Ni and Zn–Fe alloys (1.87×10^5 and 1.40×10^5 F^{-2} V^{-1}, respectively). This implies that the corrosion protection of Zn–Ni–Fe is higher than that of Zn–Ni or Zn–Fe and should result from some sort of synergistic effect of the two iron-group metals.

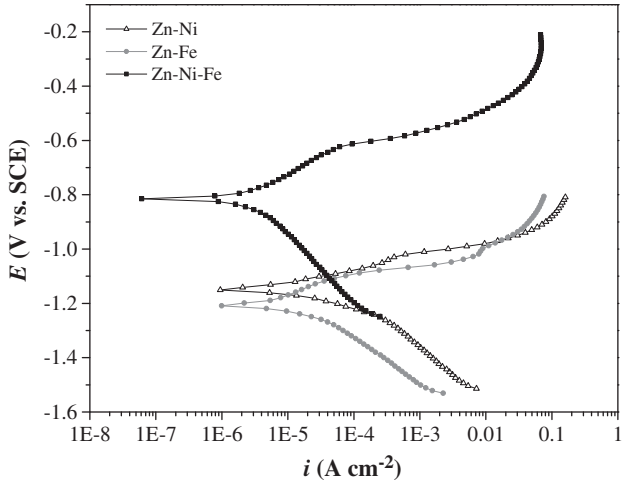

Fig. 8. Potentiodynamic polarization curves of Zn–Ni, Zn–Fe and Zn–Ni–Fe coatings, each deposited at its optimal current density. Scan rate: 1.0 mV s^{-1}.

4. Conclusions

In this work, the characteristics of the galvanostatic deposition of Zn–Ni, Zn–Fe and Zn–Ni–Fe alloys from acidic baths were compared, together with the surface morphology, phase content, chemical composition, hardness and corrosion resistance of the coatings. The following conclusions were drawn:

1. In all three alloy systems, anomalous codeposition was observed, namely the partial current density and the concentration of the less noble metal (Zn) in the coatings were the highest. The rate of Zn deposition was heavily influenced by mass-transport limitation at high applied current densities, while the rates of Ni and Fe deposition were not. In all three systems, the Faradaic efficiency was high (≥88%). As the applied current density was increased, the concentration of the nobler (iron-group) metal in the coating and the thickness of the coating increased.

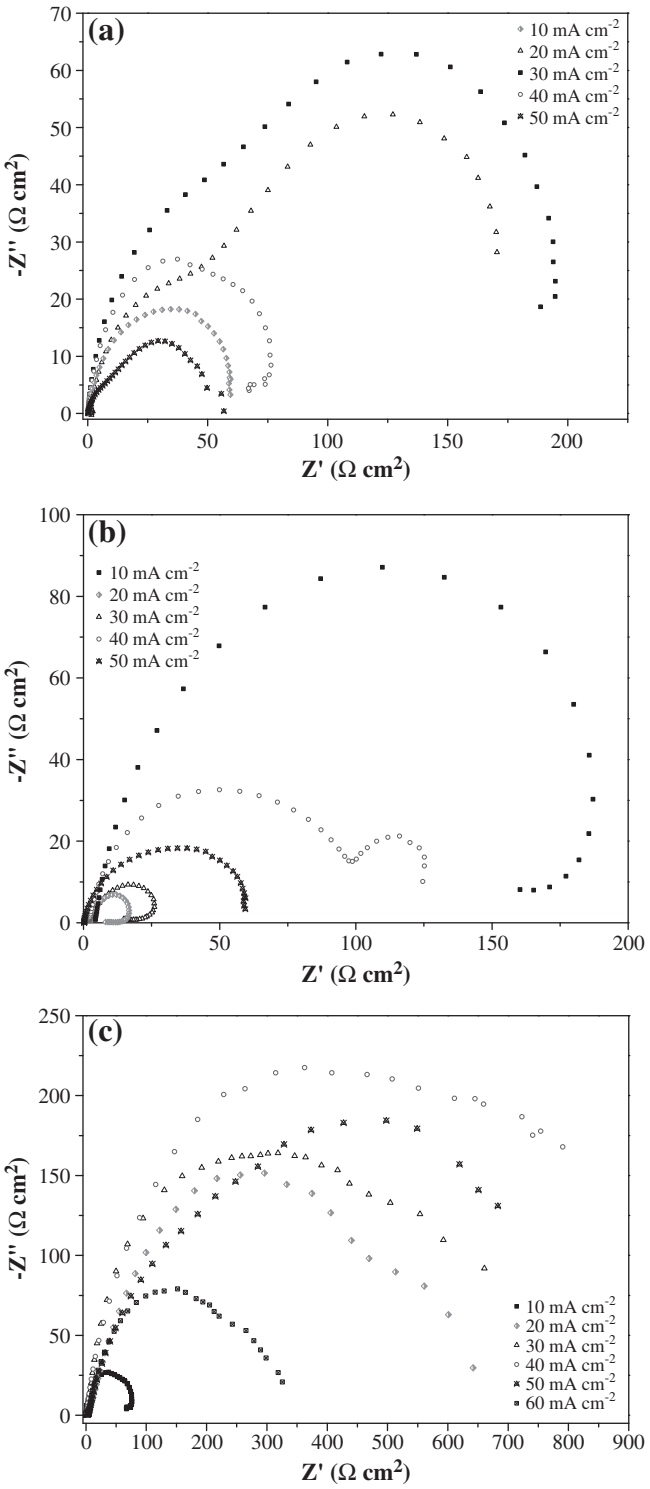

Fig. 9. EIS Nyquist spectra of (a) Zn–Ni, (b) Zn–Fe, and (c) Zn–Ni–Fe coatings, deposited at different current densities.

2. Gelatin had a more pronounced effect on deposition compared to sulfanilic acid, possibly by preferential adsorption on the surface of the cathode.
3. The hardness of the Zn–Ni coatings was the highest, while that of the Zn–Fe coatings was the lowest.
4. The lowest corrosion rate in each alloy system (214, 325 and 26 μm year^{-1} for Zn–Ni, Zn–Fe and Zn–Ni–Fe, respectively) was characteristic of coatings deposited at 30, 30 and 40 mA cm^{-2}, respectively.

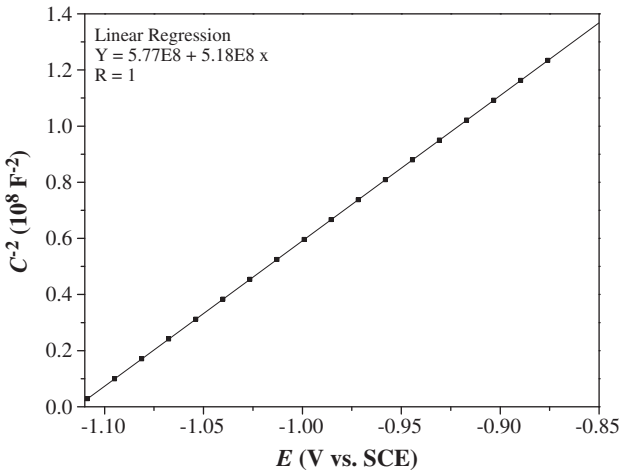

Fig. 10. Mott-Schottky plot showing *n*-type semiconductor behavior by Zn–Ni–Fe alloy deposited at its optimized current density.

5. Cyclic voltammetry revealed that the deposition of the ternary alloy had distinguished characteristics compared to that of the binary alloys. For each current density, the concentration of either Ni or Fe in the ternary alloy was higher than its corresponding concentration in the binary alloys. This means that there could be a synergistic catalytic effect due to their co-presence in solution. SEM revealed that the surface morphology of the ternary alloy was significantly different from that of the binary alloys. AFM revealed that the ternary alloy had the lowest and most uniform surface roughness. XPS and XRD revealed the presence of ZnO in the bulk of the ternary alloy coating, not just on its surface. The ternary alloy exhibited the highest corrosion potential, lowest corrosion current density, highest electrochemical impedance, and highest slope of the Mott-Schottky line. Its enhanced corrosion performance is attributed to its significantly higher content of iron-group metals, the presence of ZnO both at the surface and in the bulk, smoother surface and improved protection by the surface film, which behaves like an *n*-type semiconductor.

Acknowledgements

The authors thank Mario Levinstein from the Biomaterials and Corrosion Lab for his machinery and AFM work. We also thank Zahava Barkay, Larisa Burstein and Yuri Rosenberg from the Wolfson Applied Materials Research Center for their ESEM/EDS, XPS and XRD analyses, respectively.

References

[1] R. Fratesi, G. Roventi, G. Giuliani, C.R. Tomachuk, J. Appl. Electrochem. 27 (1997) 1088.
[2] Z.L. Wang, Y.X. Yang, Y.R. Chen, J. Corros. Sci. Eng. 7 (2005) 18.
[3] Z.F. Lodhi, J.M.C. Mol, A. Hovestad, L. 't Hoen-Velterop, H. Terryn, J.H.W. de Wit, Surf. Coat. Technol. 203 (2009) 1415.
[4] A.B. Velichenko, J. Portillo, X. Alcobé, M. Sarret, C. Müller, Electrochim. Acta 46 (2000) 407.
[5] T.V. Byk, T.V. Gaevskaya, L.S. Tsybulskaya, Surf. Coat. Technol. 202 (2008) 5817.
[6] M.S. Chandrasekar, S. Srinivasan, M. Pushpavanam, J. Solid State Electrochem. 13 (2009) 781.
[7] M. Sider, C. Fan, D.L. Piron, J. Appl. Electrochem. 31 (2001) 313.
[8] D.E. Hall, Plat. Surf. Finish. 70 (1983) 59.
[9] R. Ramanauskas, L. Gudavičiūtė, A. Kaliničenko, R. Juškėnas, J. Solid State Electrochem. 9 (2005) 900.
[10] I. Ivanov, I. Kirilova, J. Appl. Electrochem. 33 (2003) 239.
[11] V. Narasimhamurthy, B.S. Sheshadri, Met. Finish. 95 (1997) 44.
[12] R. Ramanauskas, R. Juškėnas, A. Kaliničenko, L.F. Garfias-Mesias, J. Solid State Eletrochem. 8 (2004) 416.
[13] S. Nomura, H. Sakai, H. Nishimoto, T. Uegaki, M. Sakaguchi, M. Iwai, I. Kokubo, Trans. ISIJ 23 (1983) 930.

[14] A.P. Ordine, S.L. Díaz, I.C.P. Margarit, O.R. Mattos, Electrochim. Acta 49 (2004) 2815.
[15] Y. Ohmori, K. Kondo, K. Kamei, S. Hinotani, Mater. Res. Soc. Symp. Proc. 122 (1988) 553.
[16] J.D. Jensen, D.R. Gabe, G.D. Wilcox, Surf. Coat. Technol. 105 (1998) 240.
[17] L. Felloni, R. Fratesi, E. Quadrini, G. Roventi, J. Appl. Electrochem. 17 (1987) 574.
[18] R. Albalat, E. Gómez, C. Müller, M. Sarret, E. Vallés, J. Pregonas, J. Appl. Electrochem. 20 (1990) 635.
[19] M.M. Younan, T. Oki, J. Appl. Electrochem. 26 (1996) 537.
[20] M.M. Younan, R. Ichino, T. Oki, Met. Finish. 94 (1996) 40.
[21] M.V. Ananth, N.V. Parthasaradhy, Int. J. Hydrogen Energy 22 (1997) 747.
[22] I.H. Karahan, Chin. J. Phys. 46 (2008) 105.
[23] M.M. Abou-Krisha, F.H. Assaf, S.A. El-Naby, J. Coat. Technol. Res. 6 (2009) 391.
[24] M.M. Abou-Krisha, F.H. Assaf, S.A. El-Naby, J. Solid State Electrochem. 13 (2009) 879.
[25] A. Brenner, Electrodeposition of Alloys, Vol. II, Academic Press, New York, 1963.
[26] N. Eliaz, E. Gileadi, in: C.G. Vayenas (Ed.), Modern Aspects of Electrochemistry, vol. 42, Springer, New York, 2008, p. 191.
[27] M.E. Bahrololoom, D.R. Gabe, G.D. Wilcox, J. Electrochem. Soc. 150 (2003) C144.
[28] S. Swathirajan, J. Electrochem. Soc. 133 (1986) 671.
[29] S. Lichušina, A. Chodosovskaja, A. Sudavičious, R. Juškėnas, D. Bučinskienė, A. Selskis, E. Juzeliūnas, CHEMIJA 19 (2008) 25.
[30] J.L. Ortiz-Aparicio, Y. Meas, G. Trejo, R. Ortega, T.W. Chapman, E. Chainet, P. Ozil, Electrochim. Acta 52 (2007) 4742.
[31] K. Higashi, H. Fukushima, T. Urakawa, T. Adaniya, K. Matsudo, J. Electrochem. Soc. 128 (1981) 2081.
[32] H. Yan, J. Downes, P.J. Boden, S.J. Harris, J. Electrochem. Soc. 143 (1996) 1577.
[33] M.F. Mathias, T.W. Chapman, J. Electrochem. Soc. 134 (1987) 1408.
[34] E. Gómez, E. Vallés, J. Electroanal. Chem. 397 (1995) 177.
[35] F.J. Fabri Miranda, O.E. Barcia, S.L. Diaz, O.R. Mattos, R. Wiart, Electrochim. Acta 41 (1996) 1041.
[36] R. Valotkienė, K. Leinartas, D. Virbalytė, E. Juzeliūnas, CHEMIJA 12 (2001) 236.
[37] Z.F. Lodhi, J.M.C. Mol, W.J. Hamera, H.A. Terryn, J.H.W. De Wit, Electrochim. Acta 52 (2007) 5444.
[38] N. Eliaz, T.M. Sridhar, E. Gileadi, Electrochim. Acta 50 (2005) 2893.
[39] T.M. Sridhar, N. Eliaz, E. Gileadi, Electrochem. Solid-State Lett. 8 (2005) C58.
[40] A. Naor, N. Eliaz, E. Gileadi, Electrochim. Acta 54 (2009) 6028.
[41] A. Naor, N. Eliaz, E. Gileadi, J. Electrochem. Soc. 157 (2010) D422.
[42] N. Eliaz, K. Venkatakrishna, A. Chitharanjan Hegde, Surf. Coat. Technol., doi:10.1016/j.surfcoat.2010.08.077.
[43] A.I. Vogel, Quantitative Inorganic Analysis, Longmans Green and Co, London, 1951, p. 456.
[44] K.R. Baldwin, C.J.E. Smith, M.J. Robinson, Trans. Inst. Met. Finish. 72 (1994) 79.
[45] I. Rodriguez-Torres, G. Valentin, F. Lapicque, J. Appl. Electrochem. 29 (1999) 1035.
[46] S.S.A. El Rehim, E.E. Fouad, S.M.E. El Wahab, H.H. Hassan, Electrochim. Acta 41 (1996) 1413.
[47] Bruet-Hotellaz, J.P. Bonino, A. Rousset, Marolleau, E. Chauveau, J. Mater. Sci. 34 (1999) 881.
[48] B. Szczygieł, A. Laszczyńska, W. Tylus, Surf. Coat. Technol. 204 (2010) 1438.
[49] A. Petrauskas, L. Grincevičienė, A. Češūnienė, R. Juškėnas, Electrochim. Acta 50 (2005) 1189.
[50] E. Gómez, X. Alcobe, E. Vallés, J. Electroanal. Chem. 475 (1999) 66.
[51] K. de Wit, A. de Boeck, B.C. de Cooman, J. Mater. Eng. Perform. 8 (1999) 531.
[52] C.A. Drewien, A.R. Marder, J. Mater. Sci. 29 (1994) 965.
[53] K. Kondo, S. Hinotani, Y. Ohmori, J. Appl. Electrochem. 18 (1988) 154.
[54] N.J. Cantini, D.B. Mitton, N. Eliaz, G. Leisk, S.L. Wallace, F. Bellucci, G.E. Thompson, R.M. Latanision, Electrochem. Solid State Lett. 3 (2000) 275.
[55] D.B. Mitton, S.L. Wallace, N.J. Cantini, F. Bellucci, G.E. Thompson, N. Eliaz, R.M. Latanision, J. Electrochem. Soc. 149 (2002) B265.
[56] V. Thangaraj, N. Eliaz, A.C. Hegde, J. Appl. Electrochem. 39 (2009) 339.
[57] S.B. Hong, N. Eliaz, E.M. Sachs, S.M. Allen, R.M. Latanision, Corros. Sci. 43 (2001) 1781.